Maneuver Optimization for Simultaneous Airspeed Calibration and Wind Estimation

Carlos Rubio-Sierra[1], Adrián Delgado[2], and Juan Luis Fernández-Martínez[3]

[1]Department of Aerospace Engineering, University of León, Spain. Email: carlos.rubio@unileon.es

[2]Department of Aerospace Engineering, University of León, Spain

[3]Deparment of Mathematics, University of Oviedo, Spain

Final article published in Journal of Aerospace Engineering, © ASCE, ISSN 0893-1321.
DOI: https://doi.org/10.1061/(ASCE)AS.1943-5525.0001399.

ABSTRACT

The purpose of this work is to optimize systematically the maneuver required to identify the wind and calibrate the airspeed sensor of a subsonic aircraft using a GPS method. The optimization is based on sensitivity analyses that require a considerable number of flight simulations. To face this challenging computational effort, we adapted and parallelized a particle swarm optimization algorithm. We also introduced a new formulation of the sensor model in the Bernstein form. The results show stability using the selected formulation and bring out non-obvious aliasing and precision loss effects that depend on the maneuver configuration. The knowledge of these effects allowed us to fine-tune the maneuver in order to improve the estimation's precision. Finally, we validated the method using the JSBSim flight simulator under calm and light turbulence conditions.

INTRODUCTION

Airspeed calibration is one of the most crucial processes to be performed during the flight testing of a new or modified airplane. The airspeed is for the pilot, not always human, the main variable to be known to perform a safe flight. Since the primary error contributor in the airspeed measurement is the airstream alteration caused by the plane while flying, there is no easy way to perform the calibration on the ground. The accepted methods to calibrate the airspeed measurement system are enumerated in the circular AC 23-8C (FAA 2011), applicable to small subsonic airplanes. The list includes the speed course method, tower fly-by method, trailing bomb, airspeed boom, pace airplane, as well as the GPS (Global Positioning System) methods. GPS methods are also well suited for small airplanes, like small UAVs (Unmanned Aerial Vehicles) or ultralights, since the required instrumentation can be highly miniaturized.

The GPS methods rely on evaluating the difference between the GPS measured trajectory and the one derived from the estimated model. Given that the wind during the test alters the trajectory, it should also be estimated, compensated, or ignored imposing a zero wind condition for the flight. Previous studies about airspeed calibration using GPS methods can be classified depending on the sensor model, the resolution method, and the flight maneuver. The sensor can be calibrated at individual points, as proposed by Niewoehner (2006) or using a function that represents the sensor's transfer curve. The functions that are employed vary from one to three degrees of freedom. One degree of freedom in the form of a scaling factor is used by Cho et al. (2011), Zhang et al. (2021) and Hajiyev et al. (2020), and in the form of a bias factor by Park (2017). Two degrees of freedom, in the form of a linear function, are used by Korsun et al. (2017) and Taylor (2012), and in the form of non-linear functions by Foster and Cunningham (2010) and Martos et al. (2011). Korsun and Taylor also mention the convenience of a more complex sensor model like the quadratic polynomial that Martos also employed. The resolution methods applied in the cited studies are Kalman filters or the modified version of the Newton-Raphson algorithm included in the SIDPAC (System IDentification Programs for AirCraft) (NASA 2021). The studied maneuvers are the traditional 4-leg pattern, used by Niewoehner (2006) and Martos et al. (2011), a poligonal close path (Dabney 2012), or turns with some kind of speed variation. Taylor (2012) proposes a 180-degree turn with airspeed reduction. In contrast, Foster uses a two-speed step or a continuous acceleration. Rhudy et al. (2017) and Zhang et al. (2021) also suggest circular paths. Martos et al. (2011) studies circular, race-track, and 4-leg patterns with fixed and decreasing speeds. In a corner case, when the target is to detect faults in the airspeed system instead of calibrating it, no specific maneuver is defined as in the work of Hansen and Blanke (2014).

In this paper, we propose a non previously explored formulation of the sensor model in the Bernstein form (Cargo and Shisha 1966). We consider that a minimum of three degrees of freedom is needed to model the sensor curve. Although Foster and Cunningham (2010) propose curved formulations with two degrees of freedom, they cannot be used with a sensor where the curvature is in the opposite direction, like the curve represented in (Erb 2017). Furthermore, the Bernstein form provides more meaningful and stable coefficients than the canonical base.

We also propose a new variant for the flight test maneuver consisting of a sinusoidal variation of the speed during a coordinated turn. The main contribution of the paper is the study of the maneuver using uni and bidimensional sensitivity analyses. This systematic analysis is not found in the previous literature, not only for this problem but also for other aircraft identification problems.

The resolution methods used in the past for this kind of problems are not convenient due to the great number of calculations required by the systematic sensitivity analysis. Therefore, we propose a parallelized implementation of PSO (Particle Swarn Optimization) (Kennedy' and Eberhart 1995) ready to be executed in a GPU (Graphics Processing Unit). This implementation developed *ad-hoc* for this work is based on the standard PSO algorithm (Shi and Eberhart 1998), but with a slight modification convenient for the parallel execution and which helps to control the explorative behavior of the swarm.

Finally, we validated the method using the JSBSim (Berndt et al. 2021) simulator. This simulator can reproduce the flight test in an automatable manner with the aircraft, the initial conditions, the atmosphere, the turbulence model, and the flight control system defined in script files. We tested the proposed maneuver in calm conditions to check the correspondence with the sensitivity analysis and under light turbulence to evaluate the method's precision in a real situation.

STATEMENT OF THE PROBLEM

The airspeed sensor of a subsonic aircraft derives its measurements from the dynamic pressure, i.e., the difference between the total and the static pressure. The primary source of error comes from static pressure disturbances caused by the flow field around the aircraft. This error is not easily measured on the ground, so flight testing is needed to obtain an airspeed correction curve. This airspeed calibration curve includes the effects of the different angles of attack at different speeds for a steady level flight (no sideslip and 1 G load factor). Based on the typical shape of these curves (Niewoehner 2006), (Foster and Cunningham 2010), and (Erb 2017), a quadratic polynomial (3 degrees of freedom) is appropriate to approximate it. We decided to represent the polynomial in the Bernstein form scaling the independent variable with respect to the dynamic pressure q_{max} at the VNE (Velocity Never Exceed) of the aircraft

$$q_{max} = \frac{\rho_0 \mathrm{VNE}^2}{2}, \tag{1}$$

where ρ_0 it is the sea-level density in the ISA (International Standard Atmosphere) model.

Let us define the intermediate variable t as

$$t = q/q_{max}, \tag{2}$$

and the sensor pressure error in the Bernstein form as

$$\Delta q = K_1(1-t)^2 + 2K_2 t(1-t) + K_3 t^2. \tag{3}$$

We promote the Bernstein form over the canonical one because it is more stable as does not concentrate all the defining parameters at the origin. Moreover, it provides more meaningful coefficients: K_1 representing the adjustment at the origin, K_2 the bend of the curve, and K_3 the adjustment at the maximum aircraft speed.

Once the sensor error model is established, it only remains to identify the K_1, K_2, and K_3 parameters. In order to do that, we propose a flight test consisting of a horizontal level turn with sinusoidal changing speed. The turn should be coordinated (no sideslip), and the heading change rate fixed to a low enough value to not introduce a significant load factor. The proposed formulation does not require a zero wind condition, so we also need to estimate the wind speed W_s and the wind direction W_d.

During the flight, the following variables are measured and discretized: aircraft position x, y, heading ψ, static pressure P_s, outside air temperature T, and dynamic pressure q. The variables x and y represent the position in the horizontal flight plane with a cartesian reference system centered in the first aircraft location, the x-axis pointing to the geographic north and the y-axis pointing to the east. Aircraft positions are obtained in a geodetic reference system using a GNSS (Global Navigation Satellite System) and converted to local cartesian coordinates with the transformations explained in (Eurocontrol 2005). The heading can be obtained using an on-board AHRS (Attitude and Heading Reference System) and should also be referenced to the geographic north. The static pressure and outside air temperature are used to convert the indicated airspeed to true airspeed, and finally, the dynamic pressure is measured with the airspeed sensor in calibration.

The 5-dimensional (K_1, K_2, K_3, W_s, and W_d) parameter determination problem can be solved using any global optimization algorithm able to find the parameter combination that maximizes the likelihood of the observables. In order to do that, given a random combination of the parameters, the discrete aircraft trajectory is calculated and derived a cost value as follows:

First, the aircraft dynamic pressure is obtained from the measured dynamic pressure inverting the sensor model. The sensor output q that includes the measurement error is:

$$q = q_a + \Delta q_a = q_a + K_1 \left(1 - \frac{q_a}{q_{max}}\right)^2 + 2K_2 \frac{q_a}{q_{max}} \left(1 - \frac{q_a}{q_{max}}\right) + K_3 \left(\frac{q_a}{q_{max}}\right)^2, \tag{4}$$

where q_a is the real dynamic pressure.

The inverse function is obtained solving Eq. 4 for q_a:

$$q = q_a + K_1 + K_1 \frac{q_a^2}{q_{max}^2} - 2K_1 \frac{q_a}{q_{max}} + 2K_2 \frac{q_a}{q_{max}} - 2K_2 \frac{q_a^2}{q_{max}^2} + K_3 \frac{q_a^2}{q_{max}^2},$$

$$\frac{K_1 - 2K_2 + K_3}{q_{max}^2} q_a^2 + \frac{q_{max} - 2K_1 + 2K_2}{q_{max}} q_a + K_1 - q = 0,$$

$$q_a = \frac{-\frac{q_{max}-2K_1+2K_2}{q_{max}} \pm \sqrt{\frac{(q_{max}-2K_1+2K_2)^2}{q_{max}^2} - 4\frac{K_1-2K_2+K_3}{q_{max}^2}(K_1-q)}}{2\frac{K_1-2K_2+K_3}{q_{max}^2}}.$$

Defining λ as the content of the square root and selecting the positive solution:

$$\lambda = \frac{(q_{max} - 2K_1 + 2K_2)^2 + 4(q - K_1)(K_1 - 2K_2 + K_3)}{q_{max}^2}, \tag{5}$$

therefore,

$$q_a = \frac{\frac{-q_{max}+2K_1-2K_2}{q_{max}} + \sqrt{\lambda}}{2\frac{K_1-2K_2+K_3}{q_{max}^2}},$$

$$q_a = \frac{q_{max}(2K_1 - 2K_2 + q_{max}(\sqrt{\lambda} - 1))}{2(K_1 - 2K_2 + K_3)}. \tag{6}$$

The IAS (Indicated Air Speed) and the TAS (True Air Speed) are calculated from the aircraft dynamic pressure

$$IAS = \sqrt{\frac{2q_a}{\rho_0}}, \tag{7}$$

$$TAS = \frac{IAS}{\delta}, \tag{8}$$

where δ is the density ratio with respect to the sea level, obtained as follows

$$\delta = \frac{288.15}{T + 273.15}\frac{P_s}{1013.25}. \tag{9}$$

Based on the wind speed and direction W_s,W_d, the cartesian components of the wind velocity are determined

$$W_x = W_s \sin W_d, \qquad W_y = W_s \cos W_d. \tag{10}$$

And using the aforementioned discrete variables, the aircraft trajectory is integrated, starting from the first measured location. Every location is calculated from the previous one as

$$x'_{i+1} = x'_i + (W_{x_i} + TAS_i \sin\psi_i)dt, \tag{11}$$

$$y'_{i+1} = y'_i + (W_{y_i} + TAS_i \cos\psi_i)dt, \tag{12}$$

where i is the sample index, x', y' the integrated trajectory coordinates, and dt is the sampling period.

Finally, the cost function is calculated as the sum of the distances, in norm-1, between each pair of points of the integrated and the measured trajectories

$$Z = \sum_i \left(|x'_i - x_i| + |y'_i - y_i|\right), \tag{13}$$

Norm-1 is favored over euclidean distance as it is less sensitive to outliers, although there was no significant difference between them in the simulation tests.

Based on this formulation, we have already defined the forward problem as computing the flight trajectory based on a combination of the model parameters (K_1, K_2, K_3, wind speed, and wind direction), and the measured variables (dynamic pressure, static pressure, outside air temperature, and heading). Therefore, we can define the inverse problem as determining the model parameters that best fit the observables (the GPS flight coordinates). This method is similar to the Output Error Method described by (Jategaonkar 2006) and (Klein and Morelli 2006), but minimizing the differences with the observables in norm-1 instead of norm-2 and using a different optimization method.

PROBLEM SOLUTION WITH PARALLEL PSO

A parametric study of the maneuver requires to simulate and solve a great number of synthetic flights. Besides this, nothing in the problem formulation precludes the existence of several local minimums. We selected Particle Swarm Optimization because it can be parallelized and configured

TABLE 1. Computational effort

Uni-dimensional analyses	4
Bi-dimensional analyses	6
Points per uni-dimensional analysis	200
Points per bi-dimensional analysis	441 (21x21)
Total space model points	3446
Total swarms	20676
Cost function evaluations	$\approx 3.3\text{x}10^9$
Execution time GTX 1050Ti	38.18 min
Execution time Tesla V100-SXM2	2.91 min
Estimated time GTX 1050Ti without parallelization	$\approx$ 127 days

to be explorative enough to avoid getting trapped in local minimums. The required computational effort, summarized in Table 1, justifies the development of a parallel implementation of PSO *ad-hoc* for this work. Its source code for the CUDA (Compute Unified Device Architecture) is available in (Rubio-Sierra 2020). As demonstrated in (Fernández Martínez and García Gonzalo 2008) enough explorative performance can be obtained using the standard PSO (Shi and Eberhart 1998) formulation. However, to avoid thread locks in the parallel implementation and to ease adjusting the exploration of the swarm, a separate global best is stored for each particle. Although, in this case, the PSO parameters have been considered constant, any particle of the swarm could have its own PSO parameters chosen on the neighborhood of the second-order stability limit of the trajectories (Fernandez-Martinez and Garcia-Gonzalo 2011). This feature provides a higher exploration if needed.

The position of a particle represents one combination of the estimated parameters

$$\boldsymbol{x} = \{K_1, K_2, K_3, W_s, W_d\}. \tag{14}$$

After random initialization of the particles in the search space, its movement is given by

$$v_{id}^{k+1} = c_1 v_{id}^k + c_2 U(0,1)(p_{id}^k - x_{id}^k) + c_3 U(0,1)(g_{id}^k - x_{id}^k), \tag{15}$$

TABLE 2. Parallel PSO Configuration

Parameter	Value
Inertia term c_1	0.7
Local acceleration term c_2	1.47
Global acceleration term c_3	1.47
Information factor ξ	400
Particles per swarm	800
Iterations	200
Simultaneous swarms	6

$$x_{id}^{k+1} = x_{id}^{k} + v_{id}^{k+1}, \tag{16}$$

where v is the particle speed, x its position, i the particle index, d the dimension, k the iteration, p the best position explored by the particle, g the best global, c_1 the inertia term, c_2 the local acceleration, and c_3 the global acceleration.

In each iteration, the best position explored by the particle (best local, p) and the best positions known for all the particles (best globals) are updated using the cost value from Eq. 13. Notice the existence of separated best globals g_i^k, which are updated in every iteration as the best position of a set of ξ consecutive particles starting with itself.

$$g_i^{k+1} = \text{best}\left\{g_i^k, g_{i+1}^k, ..., g_{i+\xi}^k\right\}. \tag{17}$$

Setting a small value for the ξ parameter makes the swarm more explorative while using as value the total number of particles results in the standard PSO formulation.

The configuration used is summarized in Table 2. The inertia and acceleration terms were selected to be well inside the deterministic stability region of the standard PSO algorithm, that is, the generalized PSO with $\Delta t = 1$. This stability regions are well explained in (Fernández Martínez and García Gonzalo 2008). We used a great number of particles per swarm because there is no penalty in the execution time until the thread or memory resources of one multiprocessor are

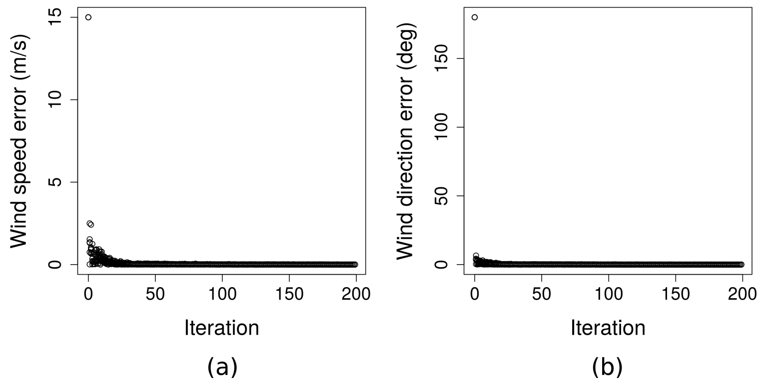

Fig. 1. Convergence of the absolute error in the wind estimation. (a) Wind speed error. (b) Wind direction error.

exhausted. The used GPU, GeForce GTX 1050 Ti, has 6 CUDA multiprocessors, so the number of simultaneous swarms was set to this number. The number of iterations was adjusted based on the convergence graphs shown in Fig. 1, Fig. 2, and Fig. 3. Finally, the information factor was set to a high value, the half number of the total particles, because as we already have many particles, we do not need to force the algorithm to be much more explorative than the standard PSO implementation.

We checked the convergence simulating a typical flight and observing the absolute error in the estimated parameters. Wind speed and direction error converge very fast, as shown in Fig. 1. In contrast, convergence for the sensor parameters K_1, K_2, and K_3 is much slower, as shown in Fig. 2, specially for K_3. Although the K_3 error graph prompts for an increase in the number of iterations, it is not necessary because the sensor parameters are an indirect measurement of the sensor precision. The purpose of calibrating the airspeed sensor is to neutralize its pressure measurement error, indeed the indicated speed error. The results of the same test for the mean absolute pressure error, the maximum pressure error, and the maximum indicated airspeed error present adequate convergence without increasing the number of iterations as shown in Fig. 3.

MANEUVER ANALYSIS

The proposed maneuver consists of a horizontal coordinated level turn. During the turn, the aircraft speed changes to obtain information at different points of the sensor error curve. This speed variation can be performed by the pilot adjusting the angle of attack and the throttle setting,

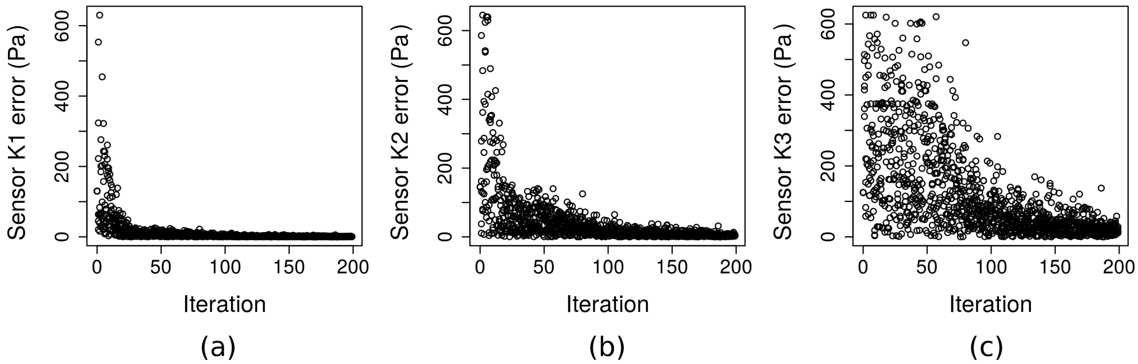

Fig. 2. Convergence of the absolute error in the sensor parameters. (a) Parameter K_1, (b) Parameter K_2. (c) Parameter K_3.

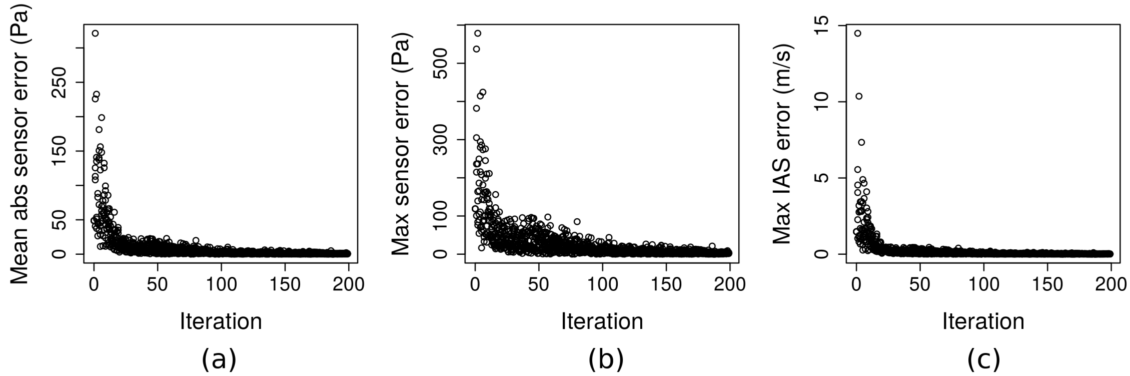

Fig. 3. Convergence of the pressure and indicated airspeed errors. (a) Mean abs pressure error. (b) Maximum abs pressure error. (c) Maximum abs airspeed error.

and it is modeled using a sinusoidal function. The heading change rate is fixed to a low value to avoid a noticeable increment of the load factor. Therefore, the maneuver has four parameters to be adjusted: the total turning angle, the mean aircraft speed, the maximum speed deviation, and the number of speed cycles.

The environmental variables, which are the static pressure, the outside air temperature, and the wind conditions, can be adjusted in a real situation only up to a certain level. The static pressure and the air temperature can be tweaked by selecting the flight altitude and the wind selecting the flight altitude and the time of the day.

The study of the maneuver is carried out systematically using unidimensional and bidimensional sensitivity analyses. The reference case needed to set the fixed variables is based on the Beechcraft

TABLE 3. Estimated Parameters Range and Reference Value

Parameter	Minimum	Maximum	Reference
Wind speed (m/s)	0	30	15
Wind direction (deg)	0	$359.\overline{9}$	180
Sensor K_1 (Pa)	-500	500	130
Sensor K_2 (Pa)	-500	500	-145
Sensor K_3 (Pa)	-500	500	-125

TABLE 4. Maneuver Parameters Range and Reference Value

Parameter	Minimum	Maximum	Reference
Total turn angle (turns)	0.5	4.0	2.0
Mean aircraft speed (m/s)	20	40	30
Aircraft speed deviation (m/s)	0	15	9
Aircraft speed cycles	0.5	4	1.5

Bonanza. The airspeed error curve for this aircraft is available in (Niewoehner 2006) and K_1, K_2, and K_3 are set to fit this curve. The speed function must be constrained so that it is always between the stall speed and the maximum horizontal speed of the airplane. The reference values and search limits used in the sensitivity analyses for the optimization of the maneuver are listed in Tables 3 and 4.

Environmental parameters correspond to a flight altitude of 3000 ft, high enough to avoid mechanical turbulence (assuming low altitude terrain), and low enough to get good aircraft performance. Moderate wind is also included in the reference case.

After establishing the reference values, we performed the uni or bidimensional sensitivity analyses varying one or two of the maneuver parameters. We evaluated the precision according to the estimation's error of: the wind speed, the wind direction, the sensor model parameters, and the derived pressure and airspeed measurements. The studied sensitivity cases comprise all the possible uni and bidimensional combinations for the four maneuver parameters. Each sensitivity analysis is performed following the next steps:

- Generate a list of combinations for the flight parameters. These combinations are the result of the cartesian product of a set for each varied variable (one variable in the uni-dimensional and two in the bi-dimensional analysis) and all the other variables in their reference values.
- For each combination, calculate the aircraft trajectory and compute the measured variables: aircraft position, heading, static pressure, outside air temperature, and dynamic pressure. The aircraft trajectory is modeled as described in the Statement of the Problem section, and the errors of the sensor are added to the dynamic pressure.
- Solve the inverse problem with the parallel PSO implementation described in the previous section.
- Calculate the precision for each estimated parameter, the mean and maximum airspeed errors (given a suitable airspeed range for the aircraft), and the mean and maximum pressure error.

The sensitivity analysis results for aircraft mean speed and speed deviation are represented in Fig. 4. Although some tendency can be observed for the aircraft's mean speed, its error values are one order of magnitude lower than the ones of the speed deviation case. Therefore, we can neglect the effects of the aircraft mean speed and focus on the selection of the deviation speed. The speed deviation for the maneuver should be selected high enough to obtain samples at most of the span of the error curve. Based on Fig. 4 (b), a minimum deviation speed of 9 m/s is appropriate. Once the deviation speed is fixed, the mean aircraft speed can be chosen using an intermediate value between the aircraft stall speed and the maximum horizontal speed to perform the required speed variation.

Regarding the number of heading turns and speed cycles, some complex interactions take place, affecting the precision of the wind and the sensor model estimation. These effects can be appreciated in Fig. 5, where we can see a lower precision when the number of the speed cycles is close to 1 or 2. These effects are a sort of aliasing problem. Let us suppose that the number of speed cycles is the same as the heading turns and that when the aircraft speed is maximum, the heading is towards the wind (therefore, when the aircraft speed is minimum exists tailwind). In this situation, an overestimation of the wind can be compensated by underestimating the sensor gain, resulting in different solutions with similar trajectories and similar costs. In the sensitivity tests, the

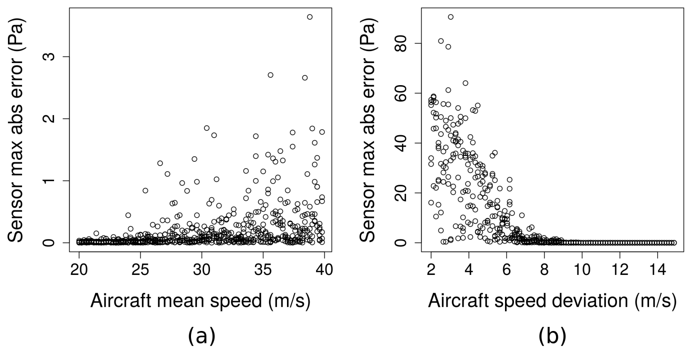

Fig. 4. Sensor maximum absolute error (Pa). (a) Sensitivity analysis for aircraft mean speed. (b) Sensitivity analysis for aircraft speed deviation.

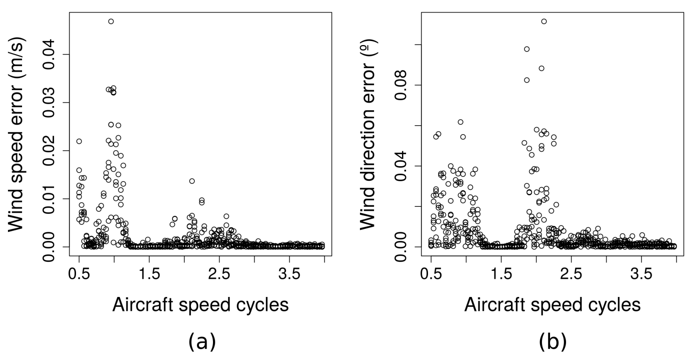

Fig. 5. Sensitivity analysis for maneuver speed cycles. (a) Wind speed error. (b) Wind direction error.

reference parameter for the heading turns was set to 2, so the loss of precision displayed in Fig. 5 occurs in the aforementioned situation and also when the number of turns is two times the number of speed cycles (second harmonic).

After checking that the relative phase between the aircraft speed and heading functions does not affect the precision, we performed the corresponding bi-dimensional sensitivity analyses. The results of these analyses, represented in Fig. 6 and Fig. 7, indicate that the aliasing effects are more complex than previously described. In the wind speed estimation, Fig. 6, the loss of precision of the first harmonic appears where it was supposed to be, in a region with a slope of 2. However, the decrease in the precision at the fundamental frequency has a slope slightly lower than 1. In the estimation of the wind direction, Fig. 7, the loss of precision related to the fundamental frequency is at the same slope as in the wind speed estimation, but the second harmonic splits into two regions.

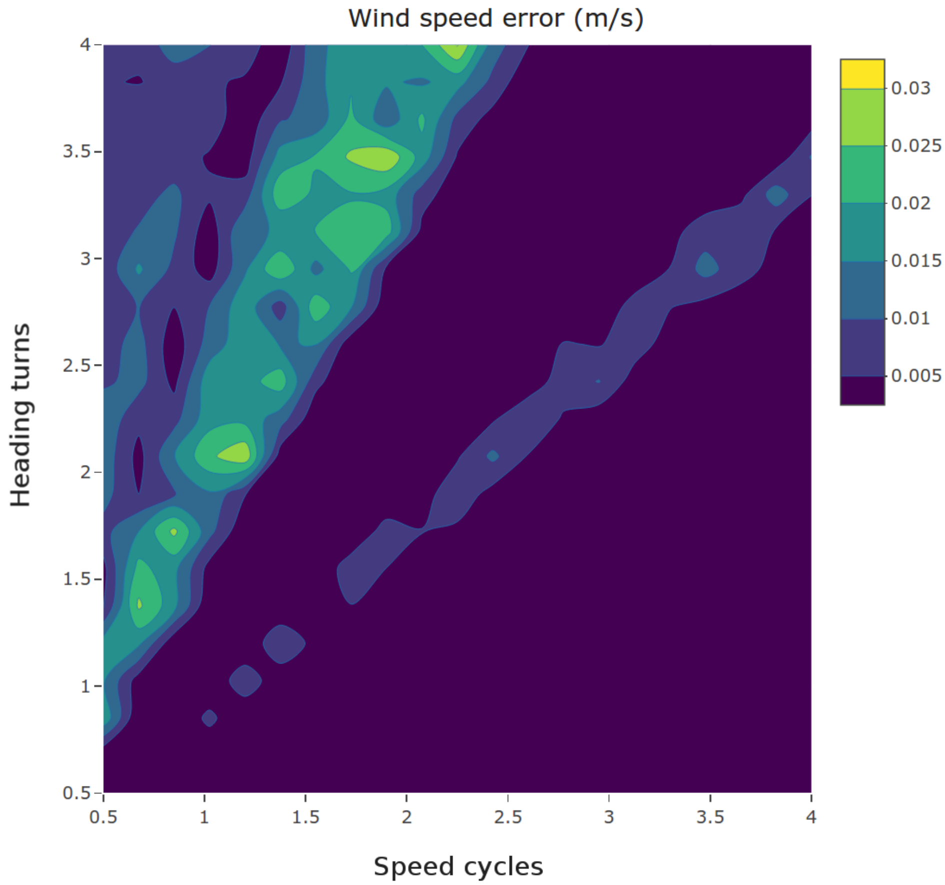

Fig. 6. Bidimensional sensitivity analysis: Wind speed estimation error vs heading turns and speed cycles.

In all the cases, the loss of precision in the wind estimation displays straight zones, which means fixed ratios between the speed cycles and the heading turns, i.e., fixed ratios between the frequencies of the speed and heading functions.

If this loss of precision in the wind estimation is caused by an aliasing effect, where the sensor model compensates the bad wind estimation, imprecisions are also expected for the sensor parameters in the same region. Fig. 8 represents the estimation error of the parameters K_1, K_2, and K_3. The expected regions are present and marked with crossed line. Not varying the aircraft speed during the maneuver thwarts the sensor model estimation because the flight test does not explore different points of the error curve. This was already analyzed when recommended a minimum deviation speed. Varying the aircraft speed extremely fast has the same effect because, in this case,

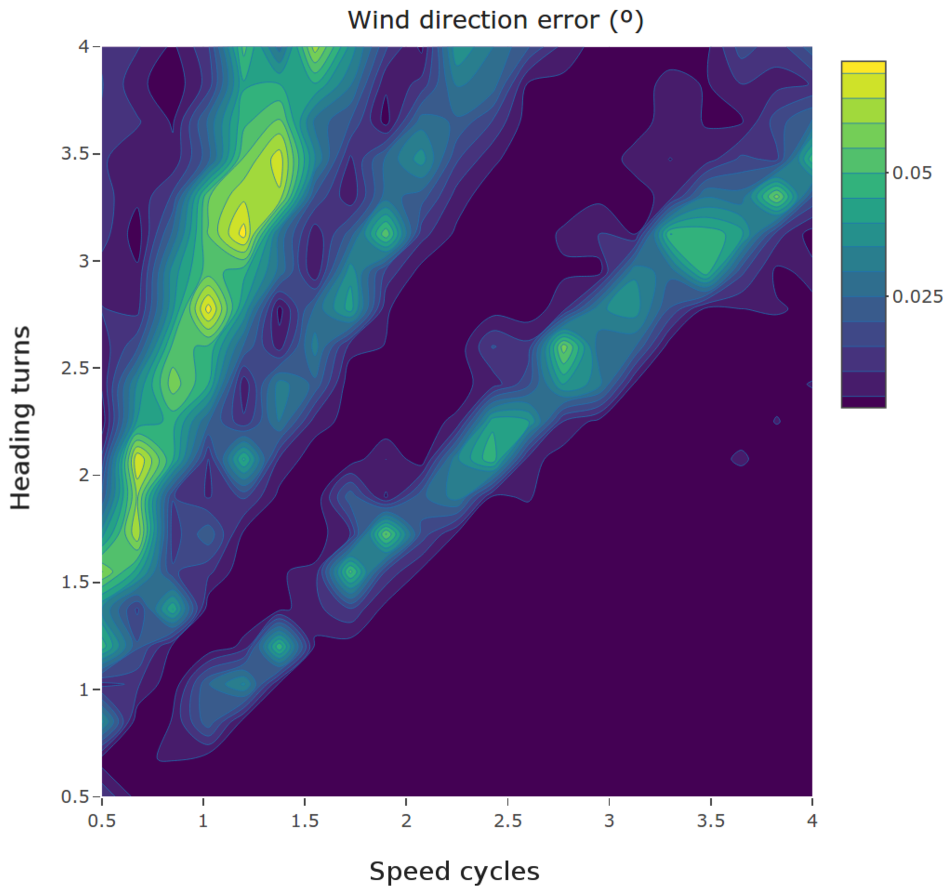

Fig. 7. Bidimensional sensitivity analysis: Wind direction estimation error vs heading turns and speed cycles.

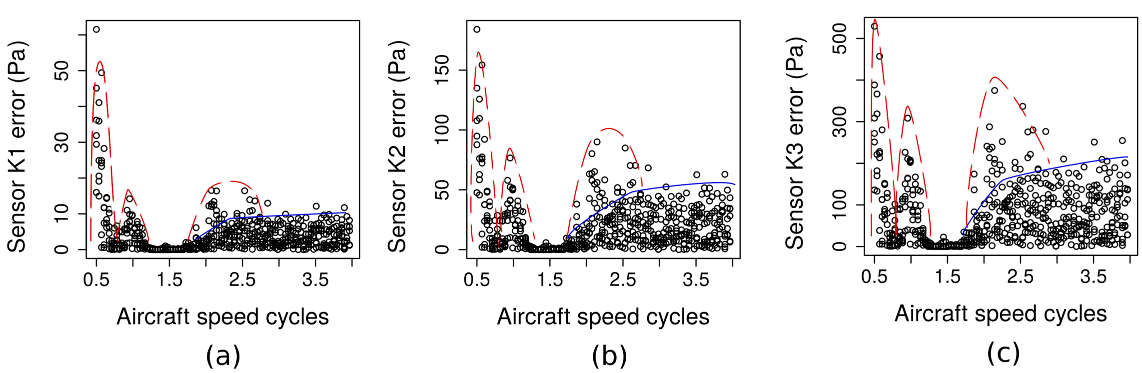

Fig. 8. Sensitivity analysis for maneuver speed cycles. In crossed line, the error regions that are caused by an inaccurate wind estimation. In continuous line, the error regions affecting only the sensor model. (a) Sensor K_1 error. (b) Sensor K_2 error. (c) Sensor K_3 error.

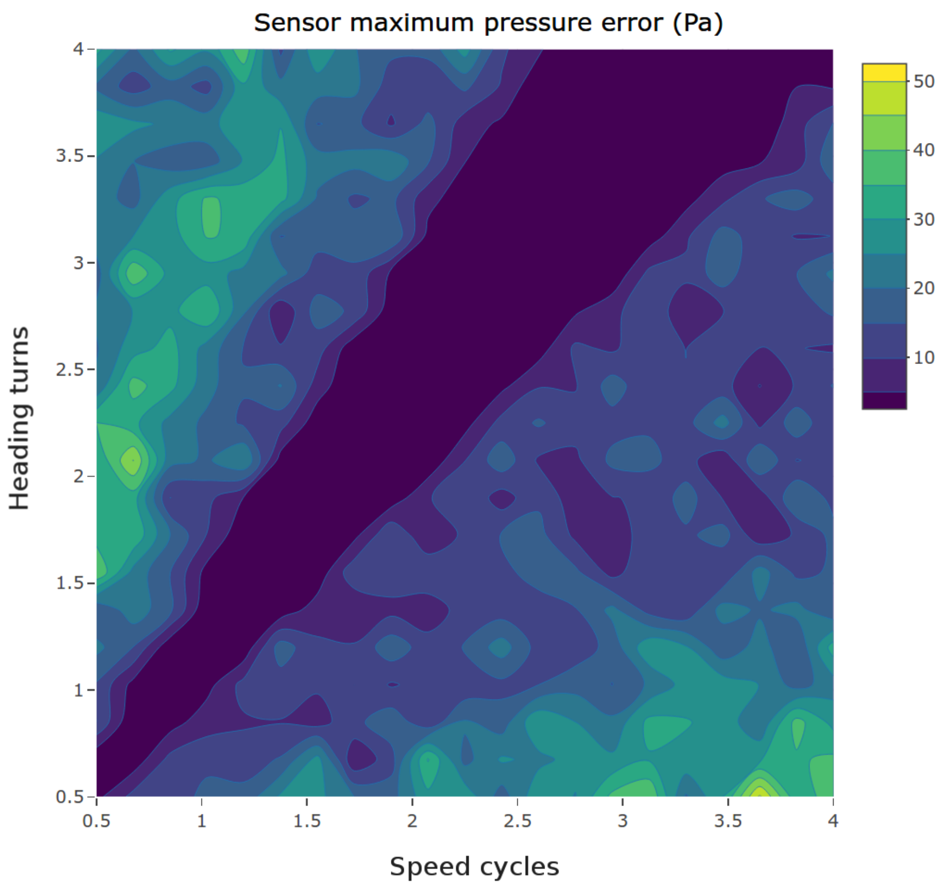

Fig. 9. Bidimensional sensitivity analysis: Sensor maximum pressure error vs heading turns and speed cycles.

we can approximate small fragments of the trajectory as if they had traveled at the mean aircraft speed. Fig. 8 shows that the loss of precision caused by changing the aircraft speed too fast starts as soon as the speed function frequency is higher than the heading function frequency. This region is marked with continuous line in the image. In the sensitivity test, the number of aircraft turns was set to 2, and being beyond this value where the error increases.

The consequences of the inaccuracies in the sensor model are errors in the measured dynamic pressure and, therefore, in the resulting indicated airspeed. The certification regulations for small airplanes FAR 23 (FAA 2020) and JAR 23 (JAA 2020) set for the airspeed sensor calibration a limit in the indicated airspeed error. Hence special interest is in analyzing the maximum pressure error and the maximum airspeed error. A bidimensional sensitivity analysis for the maximum pressure

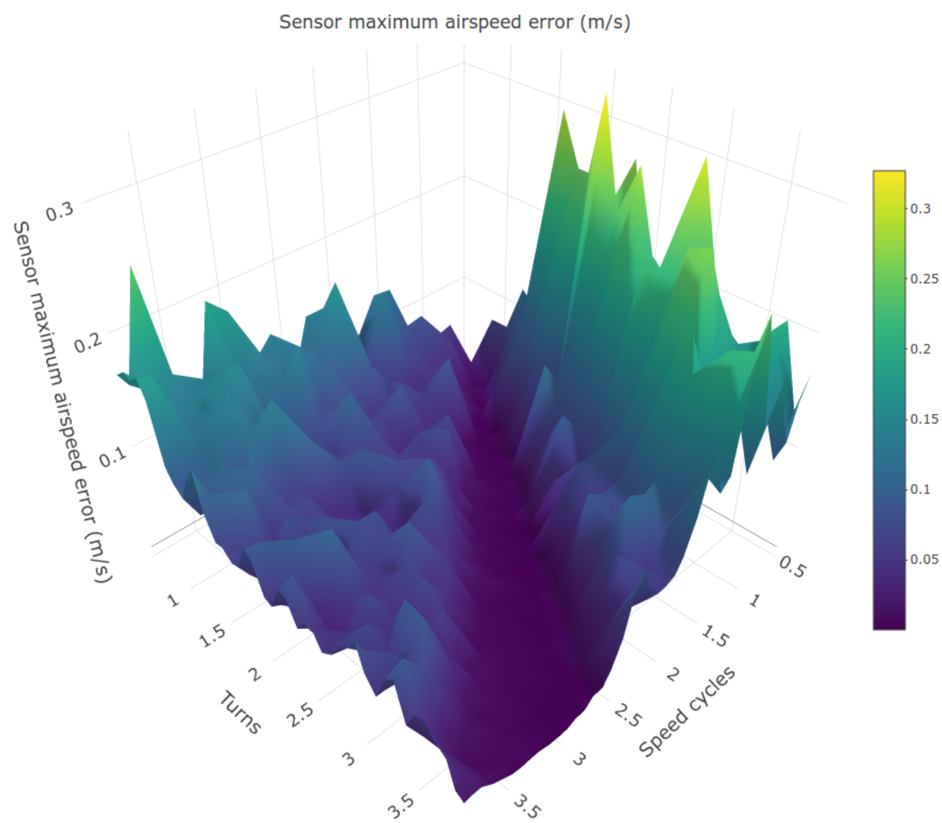

Fig. 10. Bidimensional sensitivity analysis: Sensor maximum airspeed error vs heading turns and speed cycles.

error is represented in Fig. 9. We can see that the combination of the previously described error regions results in a low error center zone. The precision degradation caused by a too fast aircraft speed variation is clearly represented in the frontier at the main diagonal. Regarding the maximum airspeed error, a similar result with a central high precision zone was obtained and represented as a surface in Fig. 10. This surface agrees with the theoretical analysis of the topography of the cost function and the effect of noise in linear and nonlinear inverse problems described in (Fernández Martínez et al. 2012), (Fernández-Martínez et al. 2014a)–(Fernández-Martínez et al. 2014b).

In summary, the flight test maneuver should have a minimum deviation speed and its aircraft mean speed can be selected freely without much impact in the estimation errors. The maneuver flight turns and speed cycles should be selected to be in the high precision valley shown in Fig. 10.

TABLE 5. Final Maneuver Configuration

Parameter	Value
Mean aircraft speed (m/s)	30
Aircraft speed deviation (m/s)	9
Total turn angle (turns)	2.5
Aircraft speed cycles	2.0

We provide a proper maneuver configuration for the studied case in Table 5.

It can be noticed that in the final maneuver configuration, the mean speed and deviation values are the same as those used as the reference in the sensitivity analyses. This is intentional, as we want the unidimensional sensitivity analysis to evaluate the loss of precision when one parameter changes with respect to the ideal maneuver.

The extremely low error in the high precision valley is unrealistic for a practical situation where there are model deviations, maneuver variations, non-constant wind, turbulence, and measurement errors. A more realistic result is represented in Fig. 11, where we modeled the wind with a 1 m/s RMS (Root Mean Square) noise in the magnitude and 1 degree RMS noise in the direction. As the errors grow due to other factors, less advantage is obtained from a perfect tuning of the maneuver. However, starting with the right one, improves the final estimation precision.

VALIDATION

JSBSim (Berndt et al. 2021) is an open-source project that provides an FDM (Flight Dynamic Model) along with the aircraft, the atmosphere, and the control devices models needed to perform a complete flight simulation. This software is also used as the engine of other flight simulators and platforms, like the FlightGear Flight Simulator or the Mixed Reality Simulation Platform. We selected JSBSim because it can be executed in accelerated time mode, launched as a batch process with all the simulation and aircraft control defined in XML files. Considering that the proposed method is suitable for the subsonic regime and that a twin-engine configuration is more stable to fly with zero sideslip in the presence of throttle changes, we selected the Cessna 310 from the list of the JSBSim available models.

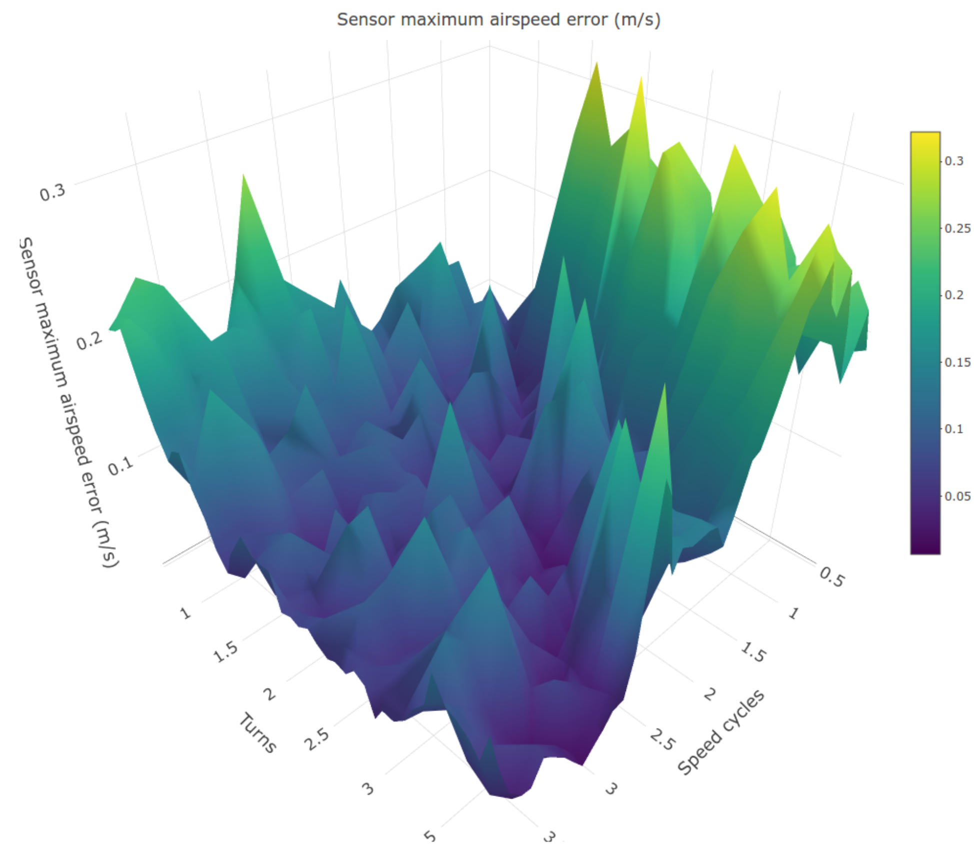

Fig. 11. Bidimensional sensitivity analysis including wind noise: Sensor maximum airspeed error vs heading turns and speed cycles.

In batch mode, the autopilot should be able to fly the required maneuver. This maneuver consists of a coordinated turn at a constant altitude with a sinusoidal airspeed variation. For the autopilot, we choose the most straightforward strategy consisting of four independent control loops, each one controlling one maneuver variable (altitude, sideslip angle, heading, and airspeed), and each one adjusting one single control (elevator, rudder, ailerons, and throttle). For the sake of completeness, we included in Annex II the four control loops. The altitude control loop, Fig. 15, is the same as the one provided by JSBSim, but with an adjustment in the Kp and Ki parameters to obtain a faster response. The same can be said for the heading control loop, Fig. 16, which is adapted from the heading hold controller provided by JSBSim. For the rudder channel, instead of using the table-based yaw damper included in JSBSim, we used a direct PID (Proportional Integral Derivative) controller to maintain the sideslip angle near zero, Fig. 17. Finally, the airspeed variation is made

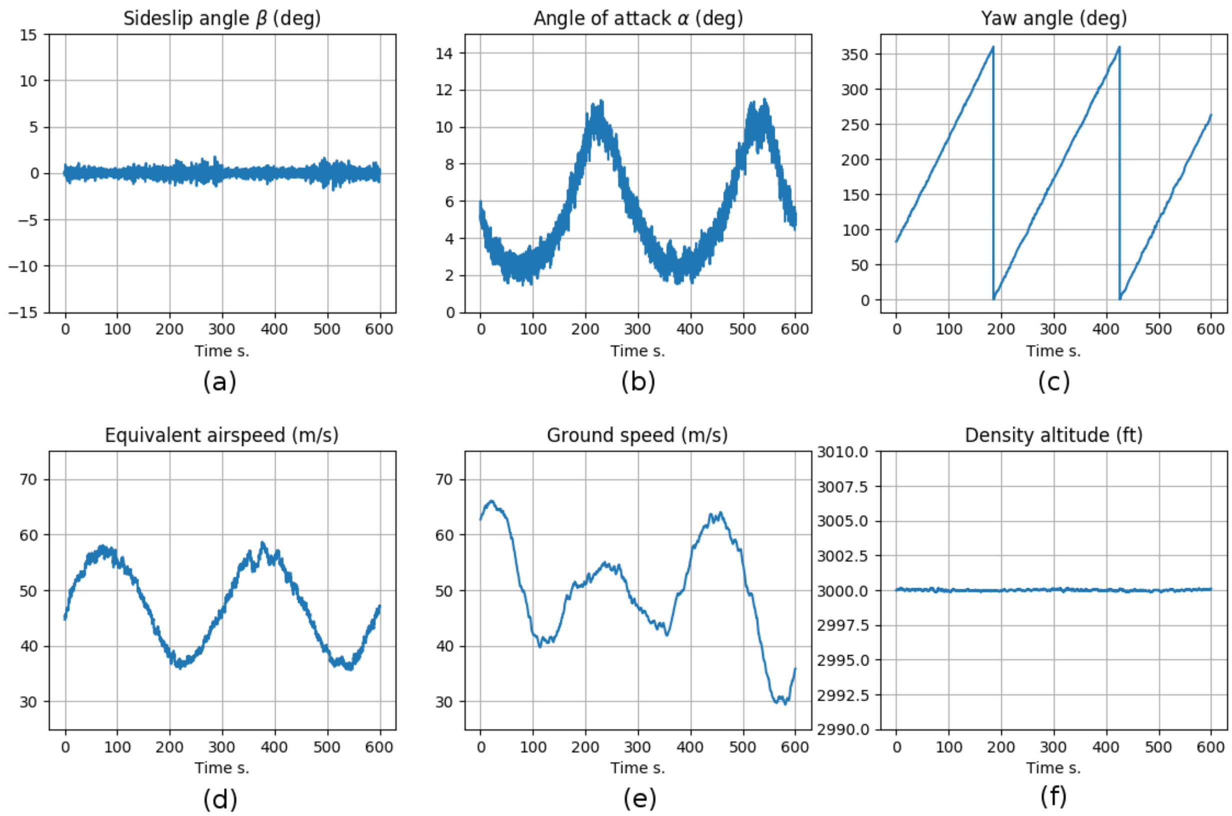

Fig. 12. Logged data from test flight with turbulence of severity level two. (a) Sideslip angle. (b) Angle of attack. (c) Yaw angle. (d) Equivalent airspeed. (e) Ground speed. (f) Density altitude

handling the throttle by another PID controller, Fig. 14. In this last control loop, we included the transformation to model the error caused by the sensor in calibration. As aforementioned, the calibration curve includes the effects of the different angles of attack at different speeds for a steady level flight, so in this transformation, we only need to add the compensation for the sideslip angle (multiply only by $\cos\beta$ and not by $\cos\alpha\cos\beta$).

We can observe the effectiveness of the control loops in the flight data represented in Fig. 12. This data corresponds to a flight that we made in turbulence conditions. The sideslip angle was in values close to zero Fig. 12(a), and altitude near the set value of 3000 ft, Fig. 12(f). The heading angle follows the expected saw tooth graph, Fig. 12(c), which corresponds to a constant increment of the heading angle. The aircraft airspeed follows the desired sinusoidal function, Fig. 12(d), with some noise produced by the atmospheric turbulence. The ground speed, Fig. 12(e), has a different

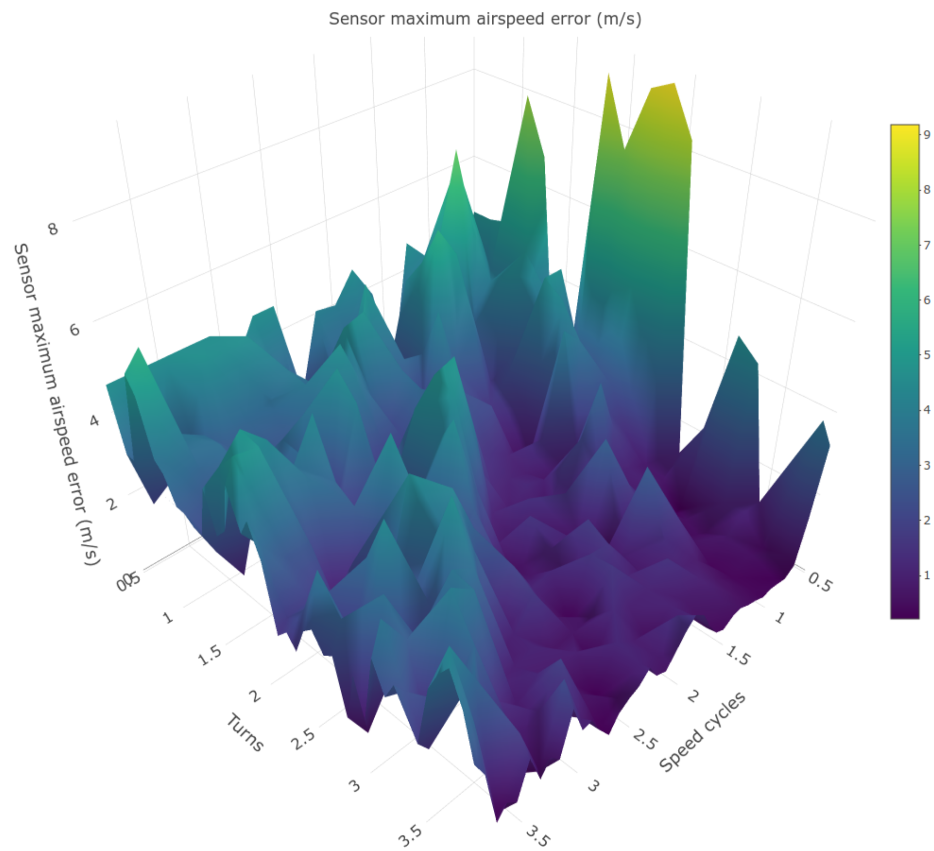

Fig. 13. Maximum airspeed error vs heading turns and speed cycles for a JSBSim test flight in air calm conditions.

shape than the airspeed (and than the true airspeed) as the aircraft is affected by a constant wind. The angle of attack, Fig. 12(b), follows an inverse shape than the airspeed as expected, where a low angle of attack corresponds to a high airspeed and vice-versa. The angle of attack is also quite affected by the turbulence.

After testing that the control loops can execute the maneuver in calm and turbulence conditions, the next step in the validation was to perform batch flights for combinations of different total turns and speed cycles. This test allow us to verify that the shape of the precission surfaces represented in Fig. 10 and Fig. 11, are also valid for a JSBSim simulated flight. The result is represented in Fig. 13, where we can see the loss of precission in the left region limited by the main diagonal and the lower error zone at the same zone that we obtained in the sensitivity analyses.

Finally, we configured the maneuver according to the sensitivity analysis results to test the

TABLE 6. Flight tests error results

	Calm conditions	Turbulence severity 1	Turbulence severity 2
Mean abs airspeed error (m/s)	0.591	0.526	0.590
Maximum abs airspeed error (m/s)	2.733	2.441	2.671
Mean abs pressure error (Pa)	18.73	16.74	18.80
Maximum abs pressure error (Pa)	61.98	54.93	60.49
Wind abs magnitude error (m/s)	0.062	0.143	0.219
Wind abs direction error (deg)	0.173	0.261	0.312

precision depending on the turbulence conditions. The maneuver was set with the values indicated in Table 5, except the mean aircraft speed that was incremented up to 46.3 m/s (90 kn) to match the Cessna 310 speed range. The turbulence model in JSBSim was set to *"ttMilspec"*. This turbulence model is described in (Yeager 1998) and implements a Dryden spectrum model with parameters according to the document MIL-F-8785C (1980). Since flight tests for airspeed calibration are usually performed on calm days, we tested only for calm conditions and turbulence with severity levels 1 and 2. The correspondence of these levels to the turbulence amplitude is represented in the Fig. 7 of MIL-F-8785C (1980). This amplitude is around 1.14 m/s (3.75 ft/s) for severity 1 and 2.13 m/s (7 ft/s) for severity 2. The magnitude of the discrete gusts also depends on the wind speed at 20 ft AGL (Above Ground Level) that was configured to 3.05 m/s (10 ft/s) for all of the tests. Table 6 shows the results of these tests. The pressure and airspeed errors were computed over the explored sensor range in the maneuver. There is no clear trend with the increase of the turbulence severity for the sensor mean and maximum errors. Therefore, the method proves to be robust, at least under light turbulence conditions. Regarding the wind estimation, we see a continuous loss of precision while the turbulence level increases, but with a very precise estimation in all the cases.

CONCLUSION

In this work, we presented a systematic study to optimize the maneuver required to identify the wind and simultaneously calibrate the airspeed sensor of an aircraft. The simulation results proved that the mathematical model is correct and that using the proposed formulation, accurate estimations can be obtained for the wind and the airspeed sensor. We modeled the sensor with a three degrees of freedom function that, in the author's opinion, is the minimum complexity in order to approximate a generic airspeed system. We used a slightly modified parallel PSO implementation as the resolution method. This method enabled performing the intensive computing required for the sensitivity analyses, and due to the random essence of the algorithm, it revealed the low precision zones in the analyses.

As a result of this study, the circumstances that cause a loss of precision depending on the maneuver parameters were identified. This allowed us to configure the optimal maneuver for this case, but actually, this article presents a general methodology for maneuver optimization that can be applied to any other aircraft identification problem.

With the help of the JSBSim simulator, we tested that the results of sensitivity analyses are congruent with the ones obtained with complete flight simulations. Finally, we evaluated the precision of the method in calm and light turbulence conditions.

DATA AVAILABILITY STATEMENT

Some or all data, models, or code generated or used during the study are available in a repository online in accordance with funder data retention policies.

The complete results of the sensitivity analyses are available at the IEEE Dataport, accessible from (Rubio-Sierra 2021a). This dataset includes the four uni-dimensional and the six bi-dimensional possible analyses of the maneuver. Regarding the bi-dimensional analyses, we also included averaged versions that compact the results of the different swarms of the same parameter combination. Scripts in R language to reproduce the plots from the data are within the dataset.

In the interest of facilitating further research and allowing to reproduce the experiments, we made open source the complete code. The CUDA PSO implementation is available in (Rubio-Sierra 2020) and the code that performs the simulations, written in Kotlin language, in (Rubio-Sierra 2021b). The JSBSim XML files needed to reproduce the validation section are also in this repository. Instructions for compile and launch the tests are within the code.

APPENDIX I. NOTATION

The following symbols are used in this paper:

c_1	=	inertia term;
c_2	=	local acceleration term;
c_3	=	global acceleration term;
g_i	=	best global position;
IAS	=	indicated airspeed (m/s);
K_1, K_2, K_3	=	sensor model coefficients;
P_s	=	static pressure (Pa);
p_i	=	best local position;
q	=	dynamic pressure (Pa);
T	=	atmosphere temperature (C);
TAS	=	true airspeed (m/s);
W_d	=	wind direction (rad);
W_s	=	wind speed (m/s);
W_x, W_y	=	wind velocity (m/s);
x, y	=	aircraft position (m);
x_i	=	particle position;
v_i	=	particle speed;
Z	=	cost value;
α	=	angle of attack (rad);
β	=	angle of sideslip (rad);
δ	=	density ratio;
ψ	=	aircraft heading (rad);
ρ_0	=	atmosphere sea-level density (Kg/m^3).

APPENDIX II. FLIGTH CONTROL

This appendix includes the diagrams of the control loops used in the JSBSim flight simulations. They consist of four independent control loops, each one controlling one aircraft command surface or the throttle.

1. The airspeed control loop, represented in Fig. 14, adjusts the throttle control based on the airspeed setpoint and the measured dynamic pressure. The airspeed setpoint follows a sinusoidal function. This control loop also includes the sensor error model.
2. The altitude control loop, represented in Fig. 15, has the mission of maintaining a constant altitude during the flight. It is similar to the one included by default in the JSBSim and sets the elevator position.
3. The heading control loop, represented in Fig. 16, is an adaptation of the heading hold controller provided in the JSBSim simulator. It controls the aileron position to follow the saw tooth function that sets a continuous increment in the heading angle.
4. The sideslip control loop, represented in Fig. 17 is a simple PID controller to maintain the sideslip angle near zero using the rudder control.

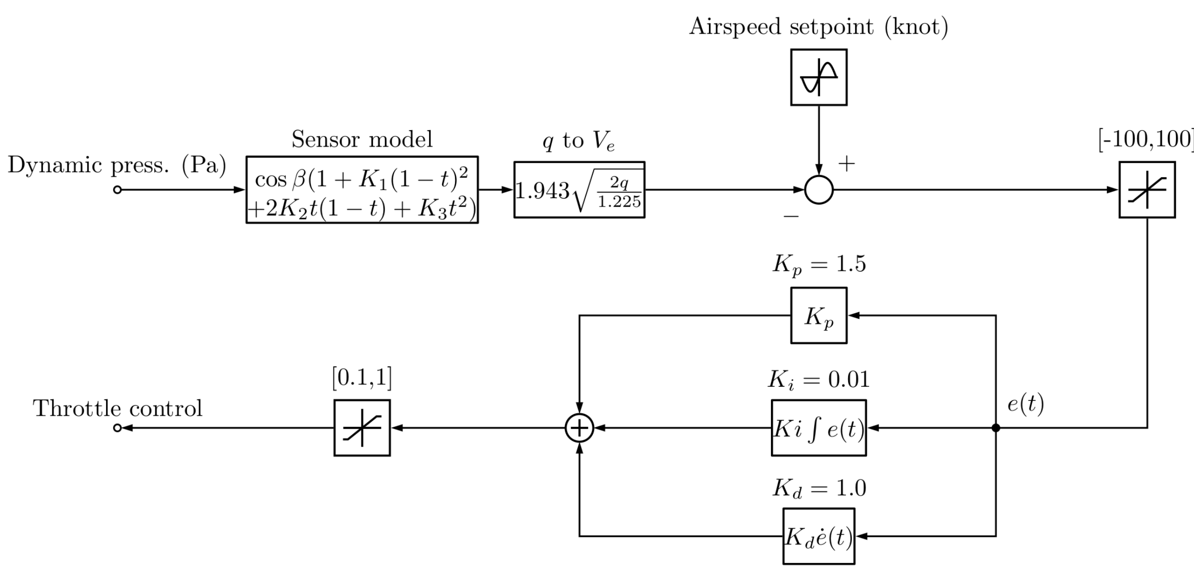

Fig. 14. Speed control.

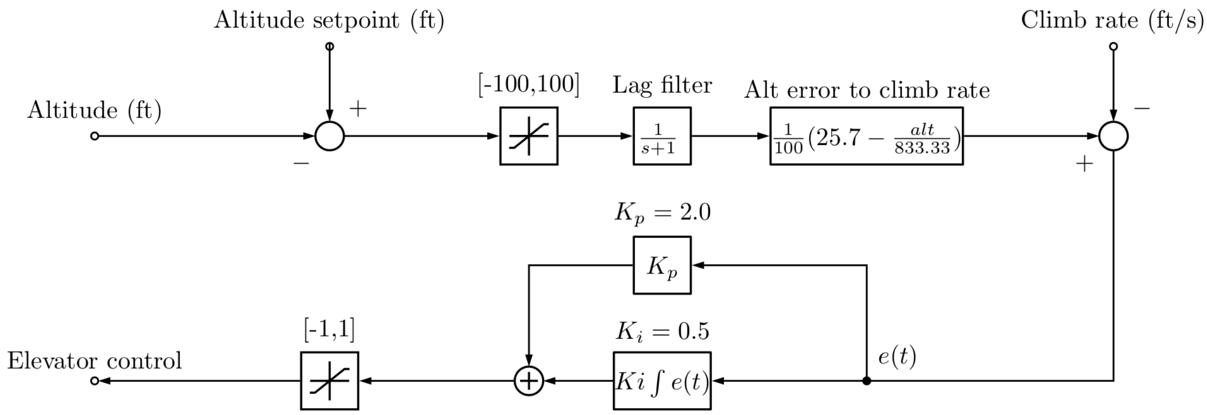

Fig. 15. Altitude control.

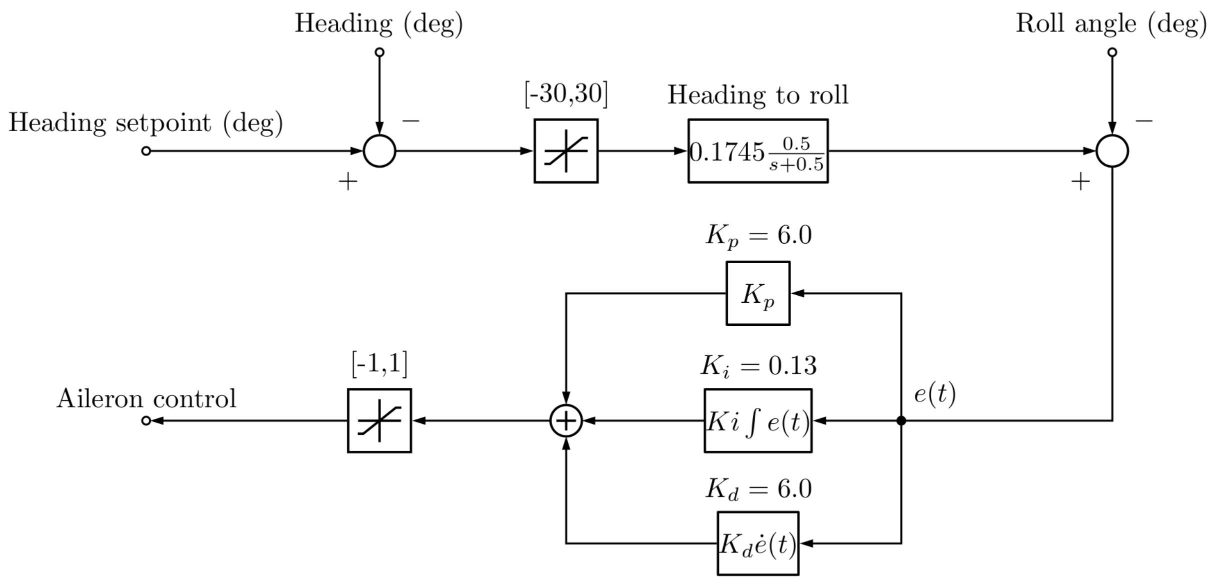

Fig. 16. Heading control.

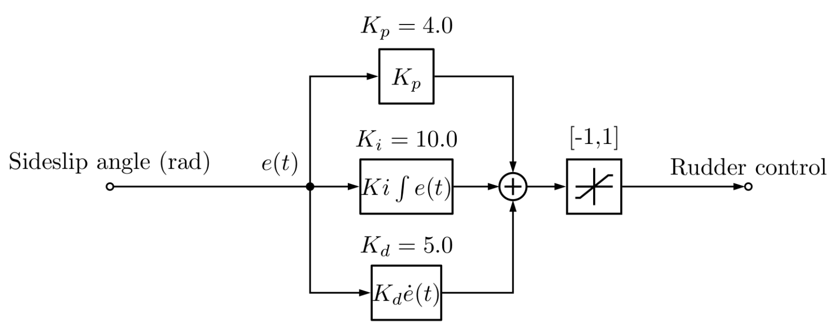

Fig. 17. Sideslip control.

REFERENCES

Berndt, J., Peden, T., Culp, D., De Marco, A., Duke, L., Froehlich, M., Megginson, D., Hofman, E., and Gidenstam, A. (2021). "JSBSim Open Source Flight Dynamics Model." *SourceForge*, <http://jsbsim.sourceforge.net/> (Jun. 21, 2021).

Cargo, G. and Shisha, O. (1966). "Bernstein form of a polynomial." *Journal of Research of the National Bureau of Standards Section B Mathematics and Mathematical Physics*, 70B(1), 79.

Cho, A., Kim, J., Lee, S., and Kee, C. (2011). "Wind Estimation and Airspeed Calibration using a UAV with a Single-Antenna GPS Receiver and Pitot Tube." *IEEE Transactions on Aerospace and Electronic Systems*, 47(1), 109–117.

Dabney, J. B. (2012). "GPS-Assisted EFIS Airspeed Calibration." *Earth and Space 2012*, Pasadena, California, United States, American Society of Civil Engineers, 1413–1422, <http://ascelibrary.org/doi/10.1061/9780784412190.150> (April).

Erb, R. E. (2017). "Dealing With the Wind: An Analysis of the Turn Regression Airspeed Calibration Technique." Florida, USA.

Eurocontrol (2005). "Coordinate Transformation Algorithms for the Hand-Over of Targets Between POEMS Interrogators." European Organisation for the Safety of Air Navigation, Brussels, Belgium.

FAA (2011). "AC_23-8C, Flight Test Guide for Certification of Part 23 Airplanes." Federal Aviation Administration, USA.

FAA (2020). "FAA Regulations. Part 23." Federal Aviation Administration, USA.

Fernandez-Martinez, J. L. and Garcia-Gonzalo, E. (2011). "Stochastic Stability Analysis of the Linear Continuous and Discrete PSO Models." *IEEE Transactions on Evolutionary Computation*, 15(3), 405–423.

Fernández-Martínez, J., Pallero, J., Fernández-Muñiz, Z., and Pedruelo-González, L. (2014a). "The effect of noise and Tikhonov's regularization in inverse problems. Part I: The linear case." *Journal of Applied Geophysics*, 108, 176–185.

Fernández-Martínez, J., Pallero, J., Fernández-Muñiz, Z., and Pedruelo-González, L. (2014b).

"The effect of noise and Tikhonov's regularization in inverse problems. Part II: The nonlinear case." *Journal of Applied Geophysics*, 108, 186–193.

Fernández Martínez, J. L., Fernández Muñiz, M. Z., and Tompkins, M. J. (2012). "On the topography of the cost functional in linear and nonlinear inverse problems." *GEOPHYSICS*, 77(1), W1–W15.

Fernández Martínez, J. L. and García Gonzalo, E. (2008). "The Generalized PSO: A New Door to PSOEvolution." *Journal of Artificial Evolution and Applications*, 2008, 1–15.

Foster, J. and Cunningham, K. (2010). "A GPS-Based Pitot-Static Calibration Method Using Global Output Error Optimization." *48th AIAA Aerospace Sciences Meeting Including the New Horizons Forum and Aerospace Exposition*, Orlando, Florida, American Institute of Aeronautics and Astronautics, <http://arc.aiaa.org/doi/10.2514/6.2010-1350> (January).

Hajiyev, C., Cilden-Guler, D., and Hacizade, U. (2020). "Two-Stage Kalman Filter for Fault Tolerant Estimation of Wind Speed and UAV Flight Parameters." *Measurement Science Review*, 20(1), 35–42.

Hansen, S. and Blanke, M. (2014). "Diagnosis of Airspeed Measurement Faults for Unmanned Aerial Vehicles." *IEEE Transactions on Aerospace and Electronic Systems*, 50(1), 224–239.

JAA (2020). "Joint Aviation Requirements. Part 23." Joint Aviation Authorities, Europe.

Jategaonkar, R. V. (2006). *Flight Vehicle System Identification: A Time Domain Methodology*. American Institute of Aeronautics and Astronautics, Inc., Reston, Virginia, USA.

Kennedy', J. and Eberhart, R. (1995). "Particle Swarm Optimization." *Proceedings of ICNN'95 - International Conference on Neural Networks*, Perth, WA, Australia, IEEE, <https://ieeexplore.ieee.org/document/488968> (November).

Klein, V. and Morelli, E. A. (2006). *Aircraft System Identification: Theory and Practice*. American Institute of Aeronautics and Astronautics, Reston ,VA, <http://arc.aiaa.org/doi/book/10.2514/4.861505> (January).

Korsun, O. N., Tulekbayeva, A. K., and Toktabek, A. A. (2017). "Estimation of errors of aircraft air parameters measurements based on satellite navigation system data." *2017 2nd*

International Ural Conference on Measurements (UralCon), Chelyabinsk, IEEE, 145–148, <http://ieeexplore.ieee.org/document/8120701/> (October).

Martos, B., Kiszely, P., and Foster, J. (2011). “Flight Test Results Of A GPS-Based Pitot-Static Calibration Method Using Output-Error Optimization For a Light Twin-Engine Airplane.” *AIAA Atmospheric Flight Mechanics Conference*, Portland, Oregon, American Institute of Aeronautics and Astronautics, <http://arc.aiaa.org/doi/10.2514/6.2011-6669> (August).

NASA (2021). “System IDentification Programs for AirCraft (SIDPAC).” *NASA Technology Transfer Program*, <https://software.nasa.gov/software/LAR-16100-1> (Jul. 26, 2021).

Niewoehner, R. J. (2006). “Refining Satellite Methods for Pitot-Static Calibration.” *Journal of Aircraft*, 43(3), 846–849.

Park, S. (2017). “Wind and Airspeed Error Estimation with GPS and Pitot-static System for Small UAV.” *International Journal of Aeronautical and Space Sciences*, 18(2), 344–351.

Rhudy, M. B., Gu, Y., Gross, J. N., and Chao, H. (2017). “Onboard Wind Velocity Estimation Comparison for Unmanned Aircraft Systems.” *IEEE Transactions on Aerospace and Electronic Systems*, 53(1), 55–66.

Rubio-Sierra, C. (2020). “CUDA framework for system identification using output error method and particle swarm optimization.” *Bitbucket*, <https://bitbucket.org/carlos-rubio/oem-cuda-pso> (Ago. 20, 2020).

Rubio-Sierra, C. (2021a). “Complete results for article: Maneuver Optimization for Simultaneous Airspeed Calibration and Wind Estimation.” *IEEE Data Port*, <http://dx.doi.org/10.21227/4y9y-4062> (Jul. 22, 2021).

Rubio-Sierra, C. (2021b). “SCG - Synthetic cases generator for sensitivity analyses.” *Bitbucket*, <https://bitbucket.org/carlos-rubio/scg> (Jul. 20, 2021).

Shi, Y. and Eberhart, R. C. (1998). “Parameter selection in particle swarm optimization.” *Evolutionary Programming VII*, G. Goos, J. Hartmanis, J. vanLeeuwen, V. W. Porto, N. Saravanan, D. Waagen, and A. E. Eiben, eds., Vol. 1447, Springer Berlin Heidelberg, Berlin, Heidelberg, 591–600. Series Title: Lecture Notes in Computer Science.

Taylor, B. (2012). “A Full-Envelope Air Data Calibration and Three Dimensional Wind Estimation Method Using Global Output-Error Optimization and Flight-Test Techniques.” *AIAA Atmospheric Flight Mechanics Conference*, Minneapolis, Minnesota, American Institute of Aeronautics and Astronautics, <http://arc.aiaa.org/doi/10.2514/6.2012-4410> (August).

US-AirForce (1980). “MIL-F-8785C, Flying Qualities of Piloted Airplanes.” Department of the Air Force, USA.

Yeager, J. C. (1998). “Implementation and Testing of Turbulence Models for the F18-HARV Simulation.” NASA, USA.

Zhang, Q., Xu, Y., Wang, X., Yu, Z., and Deng, T. (2021). “Real-Time Wind Field Estimation and Pitot Tube Calibration Using an Extended Kalman Filter.” *Mathematics*, 9(6), 646.